

DRAFT

# Characterizing the Adaptive Optics Off-Axis Point-Spread Function - I: A Semi-Empirical Method for Use in Natural-Guide-Star Observations<sup>1,2</sup>

E. Steinbring<sup>3,4</sup>, S. M. Faber<sup>5</sup>, S. Hinkley<sup>6</sup>, B. A. Macintosh<sup>7</sup>, D. Gavel<sup>7</sup>, E. L. Gates<sup>8</sup>,  
Julian C. Christou<sup>3</sup>, M. Le Louarn<sup>3,9</sup>, L. M. Raschke<sup>5</sup>, Scott A. Severson<sup>5</sup>, F. Rigaut<sup>10</sup>,  
David Crampton<sup>11,4</sup>, J. P. Lloyd<sup>12</sup>, and James R. Graham<sup>12</sup>

## ABSTRACT

Even though the technology of adaptive optics (AO) is rapidly maturing, calibration of the resulting images remains a major challenge. The AO point-spread function (PSF) changes quickly both in time and position on the sky.

---

<sup>1</sup>Based, in part, on observations obtained at the Lick Observatory, which is operated by the University of California.

<sup>2</sup>All authors except DC are affiliated with the Center for Adaptive Optics.

<sup>3</sup>Center for Adaptive Optics, University of California, Santa Cruz, CA 95064

<sup>4</sup>Visiting Astronomer, Canada-France-Hawaii Telescope, operated by the National Research Council of Canada, the Centre de la Recherche Scientifique de France, and the University of Hawaii.

<sup>5</sup>UCO/Lick Observatory, Department of Astronomy and Astrophysics, University of California, Santa Cruz, CA 95064

<sup>6</sup>Department of Physics, University of California, Santa Cruz, CA 95064. Current address: American Museum of Natural History, Department of Astrophysics, New York, NY 10024-5192

<sup>7</sup>Lawrence Livermore National Laboratory, P.O. Box 808, Livermore, CA 94551

<sup>8</sup>Lick Observatory, P.O. Box 85, Mt. Hamilton, CA 95140

<sup>9</sup>Current address: European Southern Observatory, Karl-Schwarzschild Str. 2, 85748 Garching bei München, Germany

<sup>10</sup>Canada-France-Hawaii Telescope Corporation, Kamuela, HI 96743, Current address: Gemini Observatory, 670 N. A'ohoku Place, Hilo, HI 96720

<sup>11</sup>Herzberg Institute of Astrophysics, National Research Council of Canada, Victoria, BC V9E 2E7, Canada

<sup>12</sup>Department of Astronomy, University of California, Berkeley, CA 94720

In a typical observation the star used for guiding will be separated from the scientific target by  $10''$  to  $30''$ . This is sufficient separation to render images of the guide star by themselves nearly useless in characterizing the PSF at the off-axis target position. A semi-empirical technique is described that improves the determination of the AO off-axis PSF. The method uses calibration images of dense star fields to determine the change in PSF with field position. It then uses this information to correct contemporaneous images of the guide star to produce a PSF that is more accurate for both the target position and the time of a scientific observation. We report on tests of the method using natural-guide-star AO systems on the Canada-France-Hawaii Telescope and Lick Observatory Shane Telescope, augmented by simple atmospheric computer simulations. At  $25''$  off-axis, predicting the PSF full width at half maximum using only information about the guide star results in an error of 60%. Using an image of a dense star field lowers this error to 33%, and our method, which also folds in information about the on-axis PSF, further decreases the error to 19%.

*Subject headings:* instrumentation: adaptive optics — methods: data analysis

## 1. Introduction

A key ingredient to successful analysis of images produced with the aid of an adaptive optics (AO) system is the determination of the point-spread function (PSF). The application dictates how precisely the PSF must be determined. For example, limiting the uncertainty in PSF-fitting photometry in a crowded star field to only a few percent will demand very high accuracy in knowledge of the Strehl ratio. Another example, but a case where a good reference star is less likely to be found, is the subtraction of the point-like core from the image of a quasar-host or radio galaxy (Hutchings et al. 1998, 1999; Steinbring, Crampton, & Hutchings 2002). In this case Strehl ratio may be low, and the AO PSF approximately Gaussian. For a fixed volume, the peak of a 2-dimensional circular Gaussian is inversely proportional to the square of its full-width at half maximum (FWHM). Therefore, reducing the FWHM by, say, 25% will drive the peak up by 78%. A 25% underestimate of the QSO core FWHM will have a detrimental effect on the quality of fit. In practice, accuracy of only 10% to 20% in PSF FWHM is sufficient for detection of the host galaxy.

The task of determining the PSF is made difficult by three factors. First, the performance of the AO system depends on the brightness of the star which it uses to measure correction - the “guide star.” Second, the delivered correction depends directly on quickly changing seeing conditions. Third, the AO PSF is strongly field dependent (anisoplanatic).

The first factor requires that scientific observations and calibration measurements employ either the same guide star or ones of similar brightness. Choosing a fainter guide star for calibration may require, to preserve  $S/N$ , that the AO system obtain longer integration times per measurement. Phase corrugations change continuously as the wind moves turbulence across the telescope pupil, and therefore the lower bandwidth will result in poorer correction. The latter two factors are related to the degree of turbulence along the line of sight. The seeing scales linearly with the inverse of the coherence length of phase distortions,  $r_0$  (Fried’s parameter), which for observations at zenith angle  $\gamma$ , are related to the atmospheric refractive-index structure “constant”,  $C_n^2$ , and wavelength,  $\lambda$ , by

$$r_0(\lambda, \gamma) = 0.185\lambda^{6/5} \cos^{3/5} \gamma \left( \int C_n^2(h) dh \right)^{-3/5}, \quad (1)$$

where  $h$  is height in the atmosphere (for review papers see Roddier 1981, 1999; Beckers 1983). Thus a measurement of the PSF needs to be simultaneous with the target observation or at least sample the same variation in  $r_0$ . Differences in phase distortion along different lines of sight, exacerbated by a  $C_n^2(h)$  profile skewed to high altitude, will dramatically degrade both Strehl ratio and FWHM with increasing telescope offset from the guide star. A separation of as little as  $10''$  is sufficient to render images of the guide star unusable as a PSF estimate for the target. The effect of tilt correlation also causes the off-axis PSF to be anisotropic. For any significant offset the amount of beam overlap between guide and PSF star in the tangential direction (perpendicular to the offset) will be greater than for the sagittal direction (along the offset). The lower correlation of aberrations in the sagittal direction causes the PSF to be elongated towards the guide star (see e.g. McClure et al. 1991, Voitsekovich & Bara 1999). Limited AO system bandwidth may also elongate the PSF in the direction of the prevailing wind. Thus the PSF can depend on position angle in the frame, and this requires that the PSF measurement be made near the target position as well. Figure 1 illustrates the dramatic spatial dependence of the PSF. It shows natural-guide-star AO observations of two well-separated stars, taken simultaneously (these data are discussed later, in Section 2.1). The right-hand panel is an image of the guide star and the left-hand panel is an image of a star at an offset of  $20''$ . Both images have a field of view (FOV) of roughly  $2'' \times 2''$ , and the direction to the guide star is indicated by the arrow in the left-hand panel. The on-axis image has a high Strehl ratio, greater than 30%, but the off-axis Strehl ratio is closer to 10%. Note the degradation of the off-axis PSF and its elongation towards the guide star.

If a sufficiently bright star were within a few arcseconds of the target, the task of PSF measurement would be greatly simplified. The observer could use this “PSF star” as a nearby and simultaneous measurement of the PSF during the target observation. Unfortunately, the probability that a suitably bright PSF reference will be available is very small. Furthermore, some AO systems operate with imagers originally designed for uncompensated seeing, and

their new optics have sacrificed field of view in order to obtain Nyquist sampling. For example, the small FOV such as the  $4'' \times 4''$  provided by the  $256 \times 256$  pixel Keck AO Near-Infrared Spectrometer (NIRSPEC) imager makes a fortuitous observation of both target and PSF star even more unlikely.

When faint extended objects are observed with natural guide-star AO, they will always be offset from the guide star. For a large FOV imager such as the Canada-France-Hawaii Telescope (CFHT)  $1024 \times 1024$  pixel infrared camera (KIR), the guide star is often within the  $36'' \times 36''$  FOV of the detector. This large FOV has the advantage of ensuring that a bright star will be available to characterize the on-axis PSF. Unfortunately, target integrations are typically long enough to leave a saturated image of the star. Still, several very short calibration exposures could be interleaved with those observations. An average of these would provide an unsaturated image of the star to characterize the on-axis PSF.

But even without images of the guide star, one can still determine the on-axis PSF. Consider a wave-front with corrugations consistent with a Kolmogorov spectrum. Now, consider perfect correction of the wave-front phase over an unobstructed pupil. An analytic expression can be found that gives the improvement in Strehl ratio due to successive removal of an increasing number of Zernike polynomials from the aberrated wave-front (Noll 1976). For example, removing the first 3 Zernike modes (excluding piston) corresponds to a reduction in the residual mean square wave-front distortion by a factor of 5. In a real AO system, these residual errors can in principle be determined from wave-front sensor measurements and thus used to predict the delivered on-axis PSF. The wavelengths of sensing and correction may also be different. The light from the guide star is usually split; optical light is sent to the wave-front sensor while correction is applied to the instrument light path in the near-infrared. Véran et al. (1997) have exploited this and developed software that uses wave-front information to predict the on-axis PSF in the near-infrared for the CFHT AO system.

Knowing the on-axis PSF will not give the PSF at the target position. However, an estimate of the change in the PSF with increasing offset can be determined theoretically. For the case of a single thin turbulence layer at height  $h$ , infinite telescope aperture, and perfect correction of an infinite number of modes, the off-axis Strehl ratio,  $S$ , falls as (Roddier 1999)

$$S \simeq \exp[-(\theta/\theta_0)^{5/3}] \quad (2)$$

where  $\theta$  is the offset angle on the sky, and

$$\theta_0 = 0.314 \frac{r_0 \cos \gamma}{h} \quad (3)$$

is the isoplanatic angle. For  $r_0(0.5\mu\text{m}) = 10$  cm and  $h = 2$  km this gives  $\theta_0 = 19''$  for  $K$ -band

observations at zenith. That is, the PSF at an offset of  $19''$  will have a Strehl ratio degraded by a factor of  $e$  from the on-axis value.

Determining the real AO off-axis PSF is more complicated. A real  $C_n^2(h)$  profile will contain significant power at low altitude (dome seeing, ground-layer), but the more important contribution to anisoplanaticity occurs at higher altitude. For example, measurements using SCIntillation Detection And Ranging (SCIDAR) show that a single thin high-altitude layer typically dominates the nighttime free-atmosphere  $C_n^2(h)$  profile above Mauna Kea (Racine & Ellerbroek 1995). These observations predate the use of so-called generalized SCIDAR, however, and thus do not give a true picture of the conditions at the ground layer. But, evidence from generalized SCIDAR measurements at other observatories suggest that dominance by at most a few high layers may occur elsewhere as well (cf. Klueckers et al. 1998). Equation 3 suggests that the isoplanatic angle is inversely proportional to the height of the dominant layer. In reality, the off-axis Strehl ratio will depend on the mean height of the atmospheric turbulence,  $\bar{h}$ , and on the equivalent number of corrected Zernike modes,  $N$ . Higher order modes will decorrelate more quickly than low order ones, resulting in a smaller isoplanatic angle (see e.g. Roddier 1999). That is, equation 2 should be replaced by (Flicker & Rigaut 2002)

$$S \simeq \exp[-(\theta/\theta_N)^{5/3}], \quad (4)$$

with the exponent tending towards 2 for very partial compensation (Roddier et al. 1993). The “instrumental” isoplanatic angle is then given by

$$\theta_N = 0.314 \frac{r_0 \cos \gamma}{\bar{h}}, \quad (5)$$

where (Fried 1982)

$$\bar{h} = \sec \gamma \left( \int C_n^2(h) h^{5/3} dh / \int C_n^2(h) dh \right)^{-3/5}. \quad (6)$$

Now appropriately modified, equations 4 and 5 will give an estimate of the isoplanatic angle and layer height from measurements of the off-axis Strehl ratio. In practice, these Strehl ratio measurements could be made with a calibration observation of a suitably dense star field. Unfortunately, the Strehl ratio, both on-axis and off-axis, will vary with the seeing. In fact, since the off-axis PSF depends on not just the quickly varying  $r_0$ , but also on an evolving  $C_n^2$  profile, it will vary even more rapidly, and with greater amplitude (Rigaut & Sarazin 1999). Thus, if the image is to be obtained as a mosaic, it must be completed quickly, before changes in  $r_0$  or  $\bar{h}$  can introduce objectionable inhomogeneities. This calibration measurement, plus knowledge of the on-axis PSF, could be used to predict the off-axis PSF as long as there is no significant variation in the height of the dominant turbulence layer(s) or change in the equivalent number of compensated modes.

It should be stressed that the off-axis calibration image contains degenerate information about  $\bar{h}$  and  $N$ . Furthermore, if one does not know  $r_0$  during the on-axis PSF measurement, its value of Strehl ratio is also degenerate, but in  $r_0$  and  $N$ . That is, as  $r_0$  changes so does  $N$ , which in turn affects the isoplanatic angle. Although the value of  $r_0$  can be determined from the AO system wavefront-sensor signals, thus relieving the on-axis PSF ambiguity, an independent measure of  $\bar{h}$  is more difficult to obtain. Taking SCIDAR measurements during the AO observations could provide this information, but at substantial cost and effort. However, even with the degeneracy one might obtain useful results. If a uniform and low value of  $N$  were maintained, the off-axis PSF would change very gradually with offset. Figure 1 illustrates the case where Strehl ratios are high, and small changes in  $r_0$  will dramatically affect not only the on-axis Strehl ratio, but also the spatial variation in the PSF. A “first-order” method of determining the off-axis PSF variation - one that does not account for the variation in  $N$  - may be less successful here.

In response to a need to obtain reliable off-axis PSFs for the processing of faint galaxies, one of us (ES) developed a means of providing PSF information at various field positions using calibration observations of dense star fields (Hutchings et al. 1998, 1999; Steinbring, Crampton, & Hutchings 1998; Steinbring 2001; Steinbring, Crampton, & Hutchings 2002). In this method, the observer obtains images of a dense star field once or at most a few times each night; the core of a globular cluster works best. The AO system is guided on a star of similar brightness to the one used in the target observations. Frequently, the required PSF is at an off-axis position outside the FOV of the camera, so a mosaic of the star field is generated by repositioning the telescope at successively greater off-axis distances. The goal is to obtain an unsaturated image of the guide star as well as a roughly uniform distribution of stars at many off-axis positions. Now, although the guide star in the star-field calibration image is chosen to be similar in brightness to the one used in the target observation, it is very unlikely that  $r_0$  and, thus, the delivered PSF is identical. Therefore, the full PSF reconstruction technique must fold in information about the on-axis PSF *during* the scientific observation with the star-field mosaic data.

Our method to deal with time dependence is to deconvolve the image of the dense star field with the image of the guide star in that field. We assume that the effects of field-dependent aberrations in the camera optics are small compared to anisoplanicity. We would expect, if the full image is deconvolved with a sub-image of just the guide star until the entire flux is contained within one pixel, that re-convolution with that same sub-image will reconstitute the original image. That is, the PSF at each of the off-axis star positions will be restored. Therefore, we should be able to take the deconvolved image of the star field and convolve it *with the image of the guide star from a target observation*. The result would be the image of the star field as if it were observed under the natural seeing conditions

at the time of the target observation. In this way, the image of the deconvolved star field contains the differences between the on-axis and off-axis PSFs. It is a map of the convolution kernel necessary to restore the off-axis PSFs over the field and will be referred to here as the PSF kernel map. Equations 4 and 5 suggest that the accuracy of predictions with the kernel map will decrease if the values of  $\bar{h}$  and  $N$  during construction of the mosaic differ significantly from those during the target observation. To restate this another way, the off-axis PSF cannot be exactly separated into an on-axis PSF which depends only on  $r_0$ , and an off-axis kernel which depends only on  $\bar{h}$ . Even so, we propose that the PSF kernel map is a useful approximation and that it provides a plausible method for predicting the off-axis PSF. It is not a mathematically exact method, and thus the results may depend on the deconvolution technique, number of iterations, convergence criterion, among other things. For example, deconvolution of the guide-star to a spike of one pixel in width may lead to a spatial-frequency finite-support problem. One way to remedy this would be to convolve with the updated on-axis PSF first, and then deconvolve with the guide star from the calibration field. However, we will show that variation in the atmospheric conditions during observation of the star field can account for most of the uncertainty in the results, and thus for our demonstration the details of the deconvolution are not as important.

Observation of the calibration field is difficult and time-consuming, and must be a consideration in the application of the method. If only a small number of targets are observed, i.e. at only a few offset angles, a more practical method may be to measure the kernel with binaries of the appropriate separations. This may also allow for the interleaving of calibration and scientific observations, which the scarcity of globular clusters makes more difficult. We will show, however, that even a single calibration observation taken during the night is helpful. It may be that the problem is sufficiently well constrained that if one knows the on-axis Strehl and the Strehl degradation at one point, a model dependent on  $N$  and  $\bar{h}$  will be sufficient for reconstruction of the kernel map, but we leave that work for a later paper.

A theoretical expression for PSF anisoplanatism has been derived by Fusco et al. (2000), but needs an independent measurement of  $C_n^2$  (in their example case, from thermosonde data) to provide the kernel. In this paper we focus on what results can be obtained from just a calibration image. A benefit of a semi-empirical approach is that it will apply to all AO systems. Conjugation of the AO correction to high altitude layers, such as employed in Gemini Altair, will reduce variation in the off-axis PSF, and should improve the results from our method. Multi-conjugate AO (MCAO) should lessen PSF variation even more. In MCAO, PSF uniformity is more dependent on system geometry than atmospheric conditions, and a direct measurement of the PSF kernel map may prove to be a very successful tool. This may allow field dependent deconvolution, for example.

Broad-band AO observations of dense star fields are frequently made by other observers, but almost always for scientific observations of the stars in those fields and not for calibration purposes. They are generally unusable for our analysis for one or more of the following reasons: 1. The image of the guide star is saturated. 2. The FOV of the mosaic is too small or contains too few stars. 3. Typically, a long time elapses between the observation of the guide star and the other parts of the mosaic. Variations in seeing thus render any measurement of anisoplanicity unreliable.

The work discussed here involves the observation and analysis of dense star fields for the sole purpose of calibrating the AO off-axis PSF. The observations and data reductions are outlined in Section 2. Computer simulations were used to further characterize the data and the PSF prediction method was applied to them. These analyses are found in Section 3 along with a discussion of the uncertainties in the predictions. Our conclusions follow in Section 4.

## 2. Observations and Data Reduction

Observations of dense star fields were made with two AO systems: Pueo on the 3.6 m CFHT on Mauna Kea, and the Lawrence Livermore National Labs (LLNL) AO system on the 3.0 m Shane Telescope of the Lick Observatory. Both are compact systems capable only of low-order correction - providing fewer than 100 actuators in their deformable mirrors. Both are mounted at the Cassegrain focus. However, these systems represent two very different AO designs. The Pueo is a curvature wavefront-sensing system using avalanche photo-diodes (APDs) in its sensor and employing a 19-element bimorph mirror for correction (Rigaut et al. 1998). The LLNL AO system uses a CCD-based Shack Hartmann sensor and a piezostack mirror with 61 active elements (Bauman et al. 1999).

The Pueo and Lick AO systems are also located at very different observing sites. The CFHT is at an elevation of 4200 m and benefits from the already excellent seeing of Mauna Kea. Also, the CFHT observing floor is refrigerated to obtain good dome seeing by minimizing the temperature difference between the telescope and outside air. The Shane telescope depends on passive radiation and is at an elevation of only 1350 m. As a result, the CFHT provides  $V$ -band median-seeing conditions of  $\text{FWHM} = 0''.65$ , whereas at the Shane Telescope the median seeing is over  $1''$ .

The image quality delivered by these systems depends on both atmospheric conditions and system performance. Guide stars must be selected to have sufficient brightness to operate the wave-front sensors. In practice, the LLNL system can obtain diffraction-limited



performance with a star as faint as  $V = 12$ , while the low-noise APDs of the CFHT system permit diffraction-limited performance for guide stars as faint as  $V = 14$ . Even the selection of a sufficiently bright guide star, however, does not guarantee consistent performance. For example, the encroachment of thin cirrus clouds has been seen to temporarily attenuate guide-star signals and degrade phase measurement. This causes poorer delivered correction. Furthermore, small changes in the AO systems themselves also have an effect. Two examples are variation in the setup and calibration of the optical bench in the afternoon before observing and flexure of the system due to gravity during the night. It would therefore be a very difficult task to model *in detail* the performance of either system with a computer simulation in order to compare with observations.

A journal of the observations is given in Table 1. Observations were made through  $H$  or  $K_s$  filters of globular cluster fields where archival  $V$ ,  $R$ , or  $I$ -band Hubble Space Telescope (HST) Wide-Field Planetary Camera 2 (WFPC2) images were already available. The requirement of previous WFPC2 imaging was adopted for two reasons. First, to ensure that potential guide stars were not doubles or otherwise too crowded for use with the AO system. This was impossible to determine from previous ground-based images. Second, the large  $2.6' \times 2.6'$  FOV of WFPC2 helped to provide astrometry for registration of the mosaiced AO images.

## 2.1. CFHT Pueo

The CFHT observations were made during the commissioning of Pueo in June 1996. Observations of the globular cluster M 5 were made; two observations using the same  $V = 10$  guide star were made during one night. The generation of a wide-field mosaic was made difficult by the small FOV ( $9'' \times 9''$ ) of the Montreal Near Infrared Camera (MONICA) (Nadeau et al. 1994). A mosaic pattern was used to obtain a roughly  $12''$  wide by  $30''$  long strip with the guide-star at one end. The mosaic was composed of 6 individual pointings of the telescope, with a total exposure time of 30 seconds at each. These images overlapped their neighbours by a few arcseconds, which allowed us to monitor the seeing by comparing multiple observations of the same star. Each of the complete mosaics was constructed in under 10 minutes. Figure 2 is an image of the resulting field.

The star used for guiding was bright, 4 magnitudes brighter than the faint limit for Pueo, and sufficient for optimal performance of the system. However, there was some cirrus present during the night, and this may have caused the delivered performance to fluctuate independent of seeing variation. No independent measurements of the seeing, such as those provided by a dedicated seeing monitor instrument, were available at CFHT during this

run. However, wave-front sensor telemetry was recorded automatically by Pueo. Values of  $r_0(0.5\mu\text{m}, \text{zenith})$  were estimated using the technique of Véran et al. (1997) by means of software provided on the Pueo website. Values ranged from 20 to 30 cm, consistent with median or better seeing on Mauna Kea.

## 2.2. Lick AO

Since only two observations were made with the CFHT, they provided an insufficient dataset for measuring the variation in anisoplanicity. To measure this we needed many observations of the same cluster taken over the course of an entire night. Such observations were obtained with the Lick AO system on the globular cluster M 15, as part of a program funded by the Center for Adaptive Optics to study AO PSFs.

Lick AO observations were obtained through a  $K_s$  filter with the Infrared Camera for Adaptive Optics at Lick (IRCAL) (Lloyd et al. 2000) in September 2000. The same guide star was used for all star-field observations. The small IRCAL FOV ( $19'' \times 19''$ ) required the construction of oblong mosaics much like that obtained at CFHT. In this case, three individual pointings of the telescope produced strips roughly  $20''$  wide by  $60''$  long. Figure 3 is an image of the resulting field. The exposure time at each pointing was 100 seconds, and each strip took approximately 9 minutes to complete. A total of 10 strips was obtained over two nights.

The guide star was selected because it was in a particularly dense part of M 15, but it was fainter than ideal. It was at the faint limit for Lick AO guide stars. Thus, a nearby but brighter isolated star was also observed from time to time to track optimal performance. We interleaved the mosaics of M 15 with observations of this bright star and obtained total integrations of 50 seconds with both the AO system providing full correction and tip-tilt correction only.

No seeing monitor was available at Lick. In an effort to obtain independent measures of the seeing during our run, we obtained simultaneous images of stars with a different telescope nearby on the mountain. A measurement obtained from within the same dome would have been ideal, but was impractical. We utilized the Nickel 1 m telescope, located roughly 0.5 km west of the Shane. Unfortunately, changes in telescope focus made these data unusable. We were still able, however, to determine  $r_0$  during the run. Wavefront-sensor telemetry was recorded at intervals by the AO system and used to determine  $r_0(0.5\mu\text{m}, \text{zenith})$  in a manner similar to Véran et al. (1997). The mean values were  $8 \pm 3$  cm for 14 September 2000 and  $10 \pm 3$  cm for the following night.

### 2.3. Combined Dataset

All the globular-cluster data were compared to HST WFPC2 observations of the same fields in order to determine the plate scale and orientation of the cameras. We obtained good relative astrometry of stars, with sub-pixel accuracy. The data were flat-fielded, and aperture photometry was carried out on all the sky-subtracted images.

Strehl ratios were calculated for all the stars in the following manner: The diffraction pattern for a centrally obstructed circular aperture was scaled to the pixel sampling of the camera and to a flux of unity. This image was multiplied by the total flux of each measured star, shifted to that star’s sub-pixel coordinates, and divided by the original sky-subtracted image. The ratio of the peaks gives the Strehl ratio. The shifting of the diffraction pattern is easily done (in this case, with IMSHIFT in IRAF) to sub-pixel accuracy, which will limit the error due to different pixellation in the two images. A better method may be to resample the original image by a factor of 2 or more to reduce the intra-pixel averaging, but we are mostly interested in PSFs much poorer than the diffraction limit, where this effect is less severe. A further, yet systematic error in this measurement arises due to the finite size of the photometric aperture. For our photometry this corresponds to roughly a 10% overestimate of Strehl ratio, which is a consistent bias for all measurements. The dense star fields selected provided good sampling of the spatial variation in Strehl ratio. However, photometric accuracy, and therefore, accuracy of the measurement, dropped for fainter stars and for smaller separations. We overcame this problem by selecting from each field a sub-sample of the brightest and most isolated stars. We maintained this selection throughout the analysis and obtained an uncertainty in Strehl ratio for any given star in a single frame that was not much worse than its random photometric error, or on the order of few percent.

The mosaics ideally give an instantaneous measure of the PSF over the field. Since a time lapse of several minutes occurred during the observation of each mosaic, it instead also samples a temporally varying PSF. The overlapping regions provide an estimate of this variation. The Strehl ratio of a particular star in both frames typically varied by 15% for CFHT and 20% for Lick, but some discontinuities as large as 50% occurred for Lick. The mean Strehl ratios in the CFHT and Lick data are approximately 25% and 5% respectively, which suggests the mean *absolute* uncertainty in the Strehl ratio at any position in a mosaic is about 3%.

The correction delivered by both AO systems when using bright stars was similar. The mean on-axis Strehl ratio for the CFHT observations of M 5 was 0.24. This is comparable to the average value of 0.25 obtained for the Lick observations of the bright isolated star in M 15. Note, of course, that the CFHT images were obtained in  $H$  band while the Lick images were obtained through a  $K_s$  filter. Since, to first order  $r_0 \propto \lambda^{6/5}$ , observing at redder

wavelengths with Lick compensated somewhat for its poorer seeing conditions. The value of  $r_0(0.5\mu\text{m}, \text{zenith})$  at CFHT was roughly 25 cm, while at Lick it was approximately 9 cm, or almost 3 times worse. Correcting these values of  $r_0$  to the observing wavelengths gives  $100 \pm 20$  cm and  $53 \pm 18$  cm at CFHT ( $1.6\mu\text{m}$ ) and Lick ( $2.2\mu\text{m}$ ) respectively, indicating that the effective seeing conditions are comparable, differing by less than a factor of 2.

We obtained an estimate of the instrumental isoplanatic angle,  $\theta_N$ , by a least-squares fit of equation 4 to the measurements of Strehl ratios for stars in the mosaics. The values are given in Table 1 without correction for zenith angle. The M 5 (CFHT) observations have a mean  $\theta_N(1.6\mu\text{m})$  of  $33''$ . For M 15 (Lick) it was approximately  $50''$  ( $2.2\mu\text{m}$ ) on average. Combining these values of  $\theta_N$  (after correcting for zenith angle) with measurements of  $r_0$  should yield estimates of  $\bar{h}$  via equation 5. For the observations in M 5 the mean value of  $r_0$  was approximately 25 cm, which suggests that  $\bar{h}$  was approximately 5 km at CFHT. Similarly,  $r_0 \approx 9$  cm for the observations of M 15 gives  $\bar{h} \approx 2$  km at Lick.

Since the observations of the mosaics and the bright isolated star in the M 15 Lick data were interleaved, we can get a further diagnostic of the Lick AO system performance by comparing the on-axis Strehl ratios of the two observations. The difference between that obtained with full correction during the mosaics and during observations with tip-tilt only correction of the bright isolated star is a measure of how many more Zernike modes were corrected in the mosaic observation. We found that the Strehl ratio improved, on average, from 0.01 to 0.05, a factor of 5 over tip-tilt correction alone. This suggests that we achieved correction of only a few modes beyond tip and tilt (Noll 1976). This is plausible because the guide star magnitude was near the useful limit for the Lick system.

### 3. Analysis

A goal of the observations was to relate gross changes in, say,  $r_0$  or the number of corrected modes to the accuracy of the semi-empirical PSF prediction. We therefore want to, first, model the performance of the AO systems and determine what most affects their delivered isoplanatic angles. Next, we will generate the PSF kernel maps. Finally, we will relate the accuracy of the predictions based on these maps to the stability of the atmospheric conditions and performance of the AO system.

### 3.1. Computer Modeling

A computer simulation was developed to characterize the data. It is a simple model that includes a single atmospheric layer, a circular unobstructed pupil, and ideal wavefront sensing and compensation. The simulation codes were written by one of us (SH) and are based on a simulation by Rigaut (1994). Like that code, the wavefront corrugations are due to Kolmogorov turbulence and are contained in fixed phase screens; but in our case the model of the AO system is much less sophisticated and only a single phase screen is employed. This phase-screen image can be scaled according to Fried’s parameter,  $r_0$ , and the height of the atmospheric layer,  $h$ . The telescope pupil is then superimposed at a random position in the phase screen, and the aberrations are decomposed into Zernike modes via the prescription of Noll (1976). The code simulates compensation of the phase error by summing only a small subset,  $N$ , of the measured modes, re-binning this result at lower resolution to mimic the true number of actuators in the CFHT or Lick system, and subtracting the result from the phase screen. The delivered Strehl ratio,  $S$ , is calculated at several off-axis positions using the extended Marechal approximation on the residual phase error in the phase screen. The correction is done without time delay, and thus the code simulates open-loop performance of infinite bandwidth. All the simulation steps are repeated for hundreds of iterations, and the output is the average change in Strehl ratio with offset. The values of  $r_0$ ,  $h$ , and  $N$  can then be determined by a best fit optimization to these curves. Because only  $r_0$  is directly specified by the observations (see Section 2.3), we kept  $h$  and  $N$  as free parameters in the model. We set  $N \leq 12$ , which models perfect correction of low-order modes such as tip, tilt, defocus, astigmatism, coma, and trefoil.

Figure 4 shows plots of  $S$  versus offset for the two observations at CFHT. The data are shown as filled circles, and the results of the models are overplotted as smooth curves. The best-fit models have  $h \approx 5$  km. Poorer fits were obtained with higher and lower altitudes; the results of  $h = 1$  km and  $h = 10$  km are shown. Correction was good for the first mosaic, suggesting  $N = 12$ , while for the second mosaic  $N$  is closer to 9. For these choices of parameters, the simulations suggest a value of  $\theta_N \approx 20''$  for both observations.

Figure 5 shows the results for the observations at Lick. The data are shown as filled circles. The probable cause of discontinuities in the data for observations 3 and 10 is variation in  $r_0$  during the construction of those mosaics. Several simulations are shown as smooth curves; solid curves represent a simulation with  $N = 3$ , dotted curves:  $N = 4$ , and dot-dashed curves:  $N = 5$ . Three choices of layer height are plotted for each choice of number of modes corrected. Curves corresponding to  $h$  of 1 km, 2 km, and 4 km are progressively steeper, with  $h = 4$  km being the steepest. The models suggest that, for Lick, a low number of modes were corrected by the system and the dominant layer was at an altitude between

1 km and 4 km. However, The best fit model has  $N = 3$  for mosaic 1, 2, 5, and 9. A value of  $N = 4$  is a better fit for mosaics 3, 4, 6 and 7; and mosaic 8 suggests  $N = 5$ . To within the errors of the data the best model-fits all have similar values of  $\theta_N$ , tending towards 70 arcseconds.

### 3.2. Generating PSF Kernel Maps

Each of the mosaiced images from both the CFHT and Lick datasets was deconvolved with the image of its guide star. The Lucy-Richardson algorithm was employed. Other deconvolution methods such as maximum entropy were tried, with similar results. Linear deconvolution methods may prove to be faster, but were not studied. Iterations were allowed to continue until almost all the flux in the deconvolved image of the guide star was contained within a single pixel. The following convergence criterion was adopted: iterations ceased when less than 5% of the guide star flux remained outside the one-pixel spike. This was generally achieved after a few hundred iterations. Reducing the residual to, say, 1% was much more computationally expensive, required thousands of iterations, and did not significantly improve the final results. It should be pointed out that no number of iterations will reduce the residual to zero. For example, one can imagine that if the centroid of the star is not centered on a pixel, deconvolution cannot leave a spike that is restricted to just one pixel. To help remedy this, we applied sub-pixel shifts to the images so that the guide-star was centered on a pixel. The residuals for stars at off-axis positions are all larger than that for the guide-star, and less sensitive to positional errors.

This deconvolution process generates the PSF kernel maps discussed in Section 1. The kernel changes with increasing offset from the guide star, and the degree of change indicates the severity of degradation in the off-axis PSF. Within a few arcseconds of the guide-star, the kernel can be approximated by a delta-function, but at larger offset it is more Gaussian in shape. Offsets between 20'' and 40'' are of particular interest. Despite anisoplanicity, AO still provides useful correction at these offsets. However, these offsets are larger than the typical FOV of imagers currently available with AO on large telescopes. Thus, simultaneous observation of the guide star and target is not possible, and some means of calibrating the off-axis PSF is needed.

Figure 6 shows radial plots of kernels for an offset of 25''. The kernels for the M 5 (CFHT) data are shown on the left, and two of the ten kernels for the M 15 (Lick) data are shown on the right. For the CFHT data, the filled circles represent the kernel from the first mosaic, while the open circles represent the second mosaic. For the Lick data, the filled circles represent the second mosaic and the open circles represent the eighth mosaic.

These mosaics were chosen because they represent the worst-case largest possible difference in on-axis Strehl ratio. Each datum represents a pixel, and no azimuthal averaging has been done. One-dimensional Gaussian fits to the data are overplotted for comparison. For CFHT, the FWHM of the fit is  $0''.15$ , while for Lick it is  $0''.25$ . The overlap of the filled and open circles indicates that, for both the CFHT and Lick kernels, the separate kernel estimates roughly agree. The scatter in the data is due to variation in  $r_0$  during the observation and to the elongation of the kernel towards the guide-star, but the true shape of the kernel is somewhat complicated. It is not described by, say, a simple two-dimensional Gaussian with a fixed ellipticity. For example, the wings of the CFHT kernel can be fit by a Gaussian but the same profile is too broad for the core. The wings of the Lick kernel fall off faster than a Gaussian profile. To help illustrate this, 2-dimensional representations of the CFHT and Lick kernels are inset in Figure 6. Each image is an average of the same data displayed in the plot. Note the complex asymmetric shapes of both.

We are in the process of parameterizing the variation of the kernel with field position and have collected more data with Lick AO to assist in that work. We leave that analysis for a future paper. This paper deals with the kernel maps in an empirical way and will use them directly to predict the off-axis PSF.

### 3.3. Predicting the Off-Axis PSF

A goal of the observations was to determine if the reconstruction technique outlined in Section 1 could measure the AO PSF over a large FOV and predict it under different seeing conditions. Our sample of mosaics consists of long thin strips, and therefore we cannot use them to measure a change in the PSF with varying position angle about the guide star. However, a simple test can check whether a kernel map generated with different on-axis seeing conditions can be used to find the first-order radial variation in the off-axis PSF. The test is this: reproduce the star field based on a PSF variation map generated from a different observation of that same star field. The best means of demonstrating this is to reconstruct an off-axis PSF with the use of only an image of the on-axis guide-star and the PSF kernel map. Then we can compare this reconstructed PSF with the real image of that star. For high Strehl ratios, above roughly 30%, comparison of the peak brightnesses is the proper figure of merit, because the FWHM will change little. For lower Strehl ratios, FWHM becomes more relevant. Except for the first M 5 observation, the Strehl ratio was 12% or less for all of the strips. Thus, for the most part FWHM and not Strehl ratio is a better measure of image quality for our data. We therefore normalized the predicted PSF to have the same peak intensity as the data and compared their FWHM. Our more careful discussion of errors

is left for the M 15 data, where Strehl ratio is 10% or lower.

Figure 7 shows the azimuthally averaged PSF of the guide star in M 5 (CFHT) and similarly averaged PSFs of stars at radial distances of approximately  $15''$  and  $25''$ . The filled circles represent actual data from the second mosaic while the dashed curves represent the normalized, average PSF profiles from the first mosaic. The solid line is the PSF for that location reconstructed from the PSF kernel using the first mosaic data. The dashed curves are what we would predict the PSF to be at a later point in the night if all that was available was the mosaic from earlier in the night. The model is clearly a better fit to the data than the earlier PSFs even though it underpredicts the FWHM. At an offset of  $25''$  the model predicts a FWHM 31% too small, but without the model the prediction would be in error by 120%.

Figure 8 is similar to Figure 7 but shows the azimuthally averaged PSFs for M 15 (Lick). Here a kernel map generated with the eighth M 15 mosaic was used to predict the PSFs during the second M 15 mosaic observation. These mosaics were chosen because they represent the worst-case largest possible difference in on-axis Strehl ratio. The results are qualitatively similar to those for CFHT, but here the predicted FWHM is broader than the data by 44%. Without the model, the prediction would be an underestimate and in error by 69%.

The availability of several mosaics allows us to estimate the uncertainty in predicting the PSF for the Lick data. First, each of the guide-star images was used to predict the PSF at an offset of  $25''$ , i.e. without accounting for anisoplanatism at all. The FWHM was found to be in error by 60% on average. The model was then applied. Each of the images was generated using each of the other kernel maps. Figure 9 gives results of comparing the observed and predicted FWHM for a star at an offset of  $25''$ . The error in predicted FWHM is plotted against the difference in number of corrected modes in the mosaic used for the kernel map versus the predicted mosaic. The number of corrected modes was assigned according to the determination in Section 3.1. This plot shows a clear correlation. The trend is towards over-estimating the FWHM when a mosaic with too few corrected modes is used to predict the PSF. The mosaics with highest on-axis Strehl ratios, or equivalently, the highest number of corrected modes were obtained at the lowest airmasses. This suggests that calibration observations should be taken at equivalent or lower airmasses than target observations. Following this prescription and assuming that an under-estimate and over-estimate of FWHM are equally undesirable, we can determine the mean error in predicting the PSF. If we had simply used a star at an offset of  $25''$  to predict the PSF, the mean absolute error would be 33%. For the model PSFs it is 19%; an improvement by a factor of 1.7. Note that an error of 19% in predicting the PSF is also consistent with the 25%



uncertainty in Strehl ratio for the Lick mosaics. Thus the major source of error in prediction of the PSF can be attributed to variation in AO correction, and thus plausibly to variation in  $r_0$ , during construction of the mosaics. But variation in  $r_0$  is not the only way to account for the error. Variation in  $N$  and not  $r_0$  could arise from poorer correction due to the presence of cirrus, for example. This highlights how difficult it is to make a meaningful empirical prediction, and that the best method would provide independent measurements of  $r_0$ ,  $\bar{h}$ , and  $N$ . The trend in Figure 9 suggests one path to decreasing the error. The second-order effect of lower angular decorrelation with smaller  $N$  could be measured, and an appropriate model for increasing the off-axis kernel size developed.

#### 4. Conclusions

We have discussed observations of dense star fields for the purpose of calibrating AO off-axis PSFs at CFHT and Lick Observatory. The results of our simulations suggest that a simple model with a single thin turbulence layer is a useful model for our data. For both the M 5 and M 15 observations, a dominant layer at between 2 and 5 km above the telescope and a low number of corrected modes reproduces the anisoplanicity seen in the data.

A semi-empirical technique was applied that utilizes these findings to improve the prediction of AO off-axis PSFs. The results show this simple method reduces error in the prediction of the basic radial variation in the PSF. We have insufficient data to determine if it can predict the suspected variation in anisoplanicity due to position angle about the guide star. The observations of M 15 suggest that a single calibration observation of a dense stellar field is a useful prediction of anisoplanicity over the course of a night, or even for a different night, at least for the atmospheric conditions present at Lick Observatory. Errors in prediction of FWHM with this method are approximately 19% compared to 33% without any on-axis information, and 60% without any anisoplanatic correction at all. For maximum accuracy the number of corrected modes should be similar, or larger, in the calibration image. The accuracy of determining anisoplanicity from a calibration image is limited because the effects of  $r_0$ ,  $\bar{h}$ , and  $N$  are intertwined. Better results could be realized by separating these effects through independent measurement of  $C_n^2$ .

The simulations help us understand why the method is successful, if only modestly. The dominant-layer height evidently does not change during a night or from night to night significantly enough to dramatically alter the isoplanatic patch delivered by the system. Obtaining a calibration image that measures this anisoplanicity is, however, a difficult task. A mosaiced image must be completed quickly, before variations in delivered Strehl ratio ruin the measurement. Each of our mosaics was constructed in under 10 minutes, but variation in

Strehl ratio by 15% to 50% during that time ultimately limited the accuracy of the results.

In September 2001 we again used the Lick AO system but this time employed its laser beacon to acquire more calibration observations of dense star fields. Instead of narrow strips, coverage of a large box-shaped region of sky was obtained. This will allow us to characterize anisoplanatic behavior both radially away from and azimuthally about the guide star. Future observations would also benefit from confirmatory SCIDAR measurements of the  $C_n^2$  profile.

We would like to thank the staffs of the CFHT and Lick Observatories, and for the helpful comments of the referee, Olivier Lai. ES acknowledges support from the University of Victoria Department of Physics and Astronomy. The CFHT observations and some preliminary analyses were carried out while he was a graduate student there. Portions of this work were performed under the auspices of the U.S. Department of Energy by the University of California, Lawrence Livermore National Laboratory under contract No. W-7405-Eng-48. This work was supported by the National Science Foundation Science and Technology Center for Adaptive Optics, managed by the University of California at Santa Cruz under cooperative agreement No. AST-9876783.

## REFERENCES

- Bauman, B.J., Gavel, D.T., Waltjen, K.E., Freeze, G.J., Keahi, K.A., Kuklo, T.C., Lopes, S.K., Newman, M.J., & Olivier, S.S. 1999, *Proc. SPIE*, 3762, 194
- Beckers, J.M. 1993, *Annu. Rev. Astron. Astrophys.*, 31, 13
- Flicker, R.C., & Rigaut, F. 2002, in preparation
- Fried, D.L. 1982, *JOSA*, 72, 52
- Fusco, T., Conan, J.-M., Mugnier, L.M., Michau, V., & Rousset, G. 2000, *A&AS*, 142, 149
- Hutchings, J.B., Crampton, D., Morris, S.L., & Steinbring, E. 1998, *PASP*, 110, 374
- Hutchings, J.B., Crampton, D., Morris, S.L., Durand, D., & Steinbring, E. 1999, *AJ*, 117, 1109
- Klueckers, V.A., Wooder, N.J., Nicholls, T.W., Adcock, M.J., Munro, I., & Dainty, J.C. 1998, *A&AS*, 130, 141
- Lloyd, J.P., Liu, M.C., Macintosh, B.A., Sevenson, S.A., Deich, W.T., & Graham, J.R. 2000, *Proc. SPIE*, 4008, 814

- McClure, R.D., Arnaud, J., Fletcher, J.M., Nieto, J.-L., Racine, R. 1991, PASP, 103, 570
- Nadeau, D., Murphy, D.C., Doyon, R., Rowlands, N. 1994, PASP, 106, 909
- Noll, R.J. 1976, JOSA, 66, 3, 207
- Racine, R. & Ellerbroek, B.L. 1995, Proc. SPIE, 2534, 248
- Rigaut, F., Arsenault, R., Kerr, J.M., Salmon, D.A., Northcott, M.J., Dutil, Y., & Boyer, C. 1994, Proc. SPIE, 2201, 149
- Rigaut, F., Salmon, D., Arsenault, R., Thomas, J., Lai, O., Rouan, D., Véran, J.P., Gigan, P., Crampton, D., Fletcher, J.M., Stilburn, J., Boyer, C., & Jagourel, P. 1998, PASP, 110, 152
- Rigaut, F., & Sarazin, M. 1999, in ESO/OSA Proc. *Astronomy with AO: Present Results and Future Programs*, ed. D. Bonaccini, 56, 383
- Roddier, F. 1981, in Progress in Optics, 19, North-Holland, ed. E. Wolf, 281
- Roddier, F., Northcott, M., Graves, J., McKenna, D., & Roddier, D. 1993, JOSA, 10, 957
- Roddier, F. 1999, in Adaptive Optics in Astronomy, Cambridge University Press, New York, ed. F. Roddier
- Steinbring, E. 2001, PhD dissertation, Univ. of Victoria
- Steinbring, E., Crampton, D., & Hutchings, J.B. 2002, ApJ, 569, 611
- Steinbring, E., Crampton, D., & Hutchings, J.B. 1998, BAAS, 30(4), 1280
- Véran, J.-P., Rigaut, F., Maître, H., & Rouan, D. 1997, JOSA A, 14(11), 3057
- Voitsekhovich, V.V., & Bara, S. 1999, A&AS, 137, 385

Table 1. Journal of Observations

							AO Correction				
							Guide		Full		Tip-Tilt
									$S$ (on-axis)	$\theta_N$ (arcsec)	$S$ (on-axis)
Object	UT	$V$ (mag)	Exp. (s)	Air.	$r_0(0.5\mu\text{m}, 0^\circ)$	$S$ (on-axis)	$\theta_N$ (arcsec)	$S$ (on-axis)			
CFHT Pueo/MONICA $H$											
M 5, 1	25/06/1996 06:06	10	30	1.12	$30 \pm 5$	0.36	$33 \pm 2$	...			
M 5, 2	07:26	10	30	1.05	$20 \pm 5$	0.12	$34 \pm 5$	...			
Lick AO/IRCAL $K_s$											
M 15 PSF	14/09/2000 04:07	8	50	1.26	$8 \pm 3$	0.19	...	0.01			
M 15, 1	04:55	12	100	1.15		...	$82 \pm 59$	...			
M 15, 2	05:47	12	100	1.11		0.02	$53 \pm 16$	...			
M 15 PSF	06:28	8	50	1.11		0.22	...	0.01			
M 15, 3	07:11	12	100	1.14		0.03	$53 \pm 13$	...			
M 15, 4	08:03	12	100	1.24		0.05	$47 \pm 9$	...			
M 15 PSF	08:42	8	50	1.37		0.18	...	0.01			
M 15, 5	09:55	12	100	1.83		0.04	$56 \pm 14$	...			
M 15 PSF	15/09/2000 04:18	8	50	1.20	$10 \pm 3$	0.12	...	0.01			
M 15, 6	05:00	12	100	1.14		0.07	$42 \pm 6$	...			
M 15, 7	05:51	12	100	1.11		0.06	$48 \pm 9$	...			
M 15 PSF	06:25	8	50	1.11		0.31	...	0.01			
M 15, 8	07:10	12	100	1.14		0.08	$46 \pm 9$	...			
M 15, 9	08:05	12	100	1.26		0.03	$65 \pm 17$	...			
M 15 PSF	08:43	8	50	1.40		0.50	...	0.03			
M 15, 10	09:53	12	100	1.81		0.06	$53 \pm 10$	...			

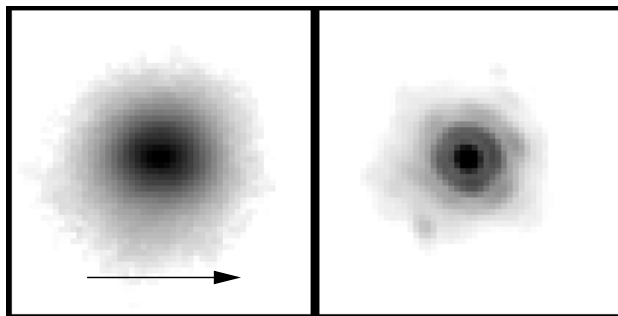


Fig. 1.— Simultaneous AO observations of two well-separated stars. The image of the guide star is shown on the right, and the image of a star at an offset of  $20''$  is shown on the left. Both images are displayed with the same log grey-scale, and have a FOV of roughly  $2'' \times 2''$ . The direction to the guide star is indicated by the arrow in the left-hand panel. The effects of anisoplanatism and anisotropy have degraded the off-axis PSF and elongated it towards the guide star.

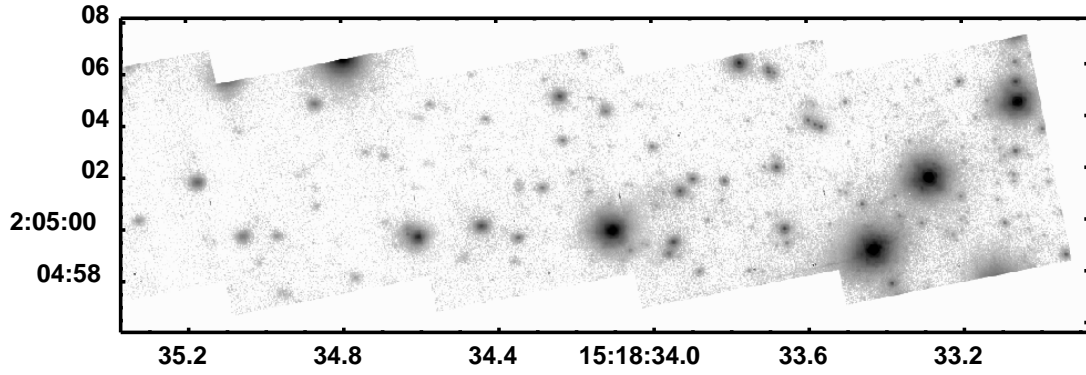


Fig. 2.— A single mosaiced strip from the CFHT Pueo (M 5) dataset. North is up and east left in this log grey-scale image. Right ascension and declination are given in J2000.0 coordinates. The guide star is on the right, the central member of the group of three bright stars.

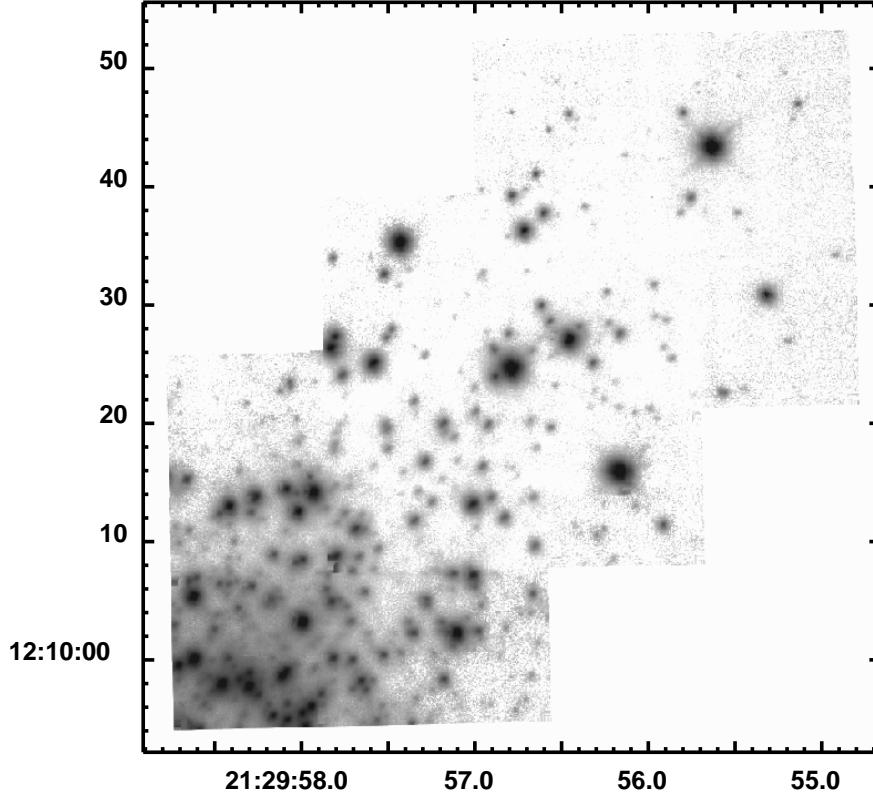


Fig. 3.— A single mosaiced strip from the Lick AO (M 15) dataset. North is up and east left in this log grey-scale image. Right ascension and declination are given in J2000.0 coordinates. The guide is the bright star at upper right. Notice the increased crowding toward the lower left in the image, which is in the direction of the M 15 core. These stars were too crowded for good photometry, which made much of the data from this region unusable.

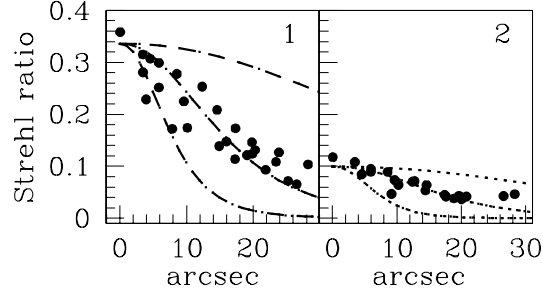


Fig. 4.— Plots of the Strehl ratio as a function of off-axis angle for two observations of M 5 (CFHT). The filled circles are the data from mosaics 1 and 2. The curves represent the model results: dotted for 8 corrected modes (mosaic 2) and dot-dashed for 11 corrected modes (mosaic 1). The best-fit models have  $h = 5$  km. Models for 1 km and 10 km are also shown, the latter indicated by the steepest curve.



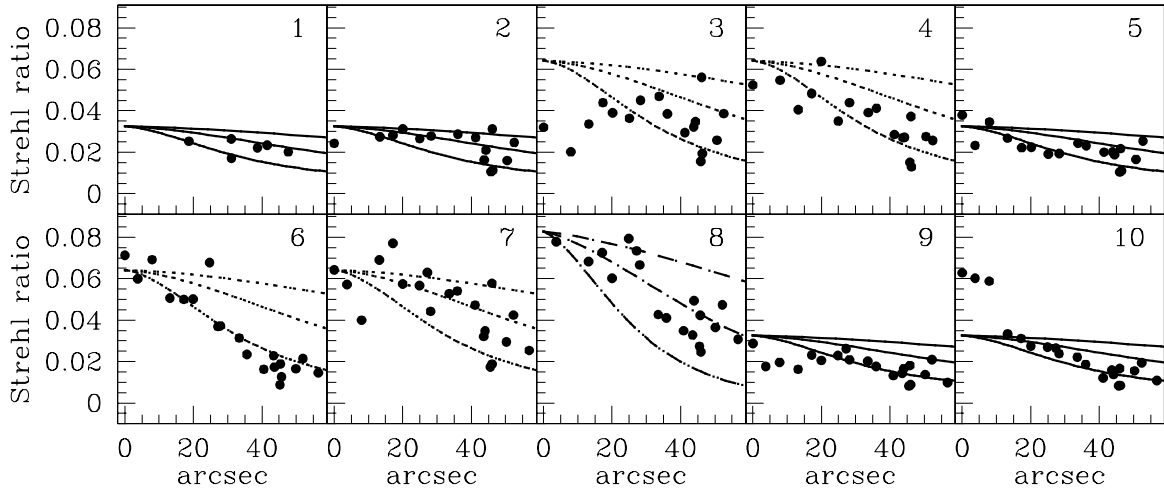


Fig. 5.— Plots of the Strehl ratio as a function of offset for ten observations of M 15 (Lick). Mosaics 1 through 5 were obtained sequentially over 5 hours on 14 September 2000, while 6 through 10 were obtained similarly the next night. Note the strong discontinuities in the data for mosaics 3 and 10. In both cases this discontinuity occurs at the boundary between data obtained at two separate telescope pointings, and thus a plausible explanation is variation of  $r_0$  with time. The curves represent the model results: solid for 2 corrected modes, dashed for 3 corrected modes, and dot-dashed for 4 corrected modes. Each of these is further separated into models with atmospheric-layer heights of 1 km, 2 km, and 4 km; the last indicated by the steepest curve.

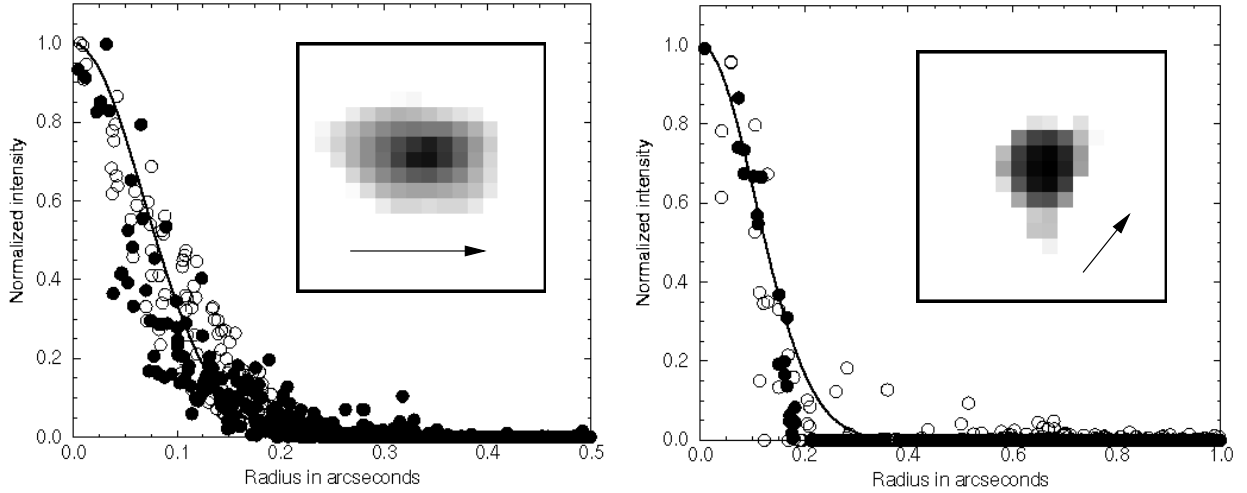


Fig. 6.— Plots of the kernel at an offset of  $25''$  for the M 5 data (CFHT, left) and M 15 data (Lick, right). Each data point represents a pixel in the image. For the M 5 data, the filled circles represent the kernel from the first mosaic, while the open circles represent the second mosaic. For the M 15 data, the filled circles represent the second mosaic and the open circles represent the eighth mosaic. Gaussian fits to the data are overplotted as solid lines. Two-dimensional representations of the CFHT and Lick kernels are inset. Each is the average of the same data shown in the plot. The images have a FOV of  $0''.5 \times 0''.5$  (CFHT) and  $1'' \times 1''$  (Lick) and are displayed with a log grey-scale. The direction to the guide star is indicated by an arrow. The CFHT and Lick kernels have a different, complex asymmetric shape.

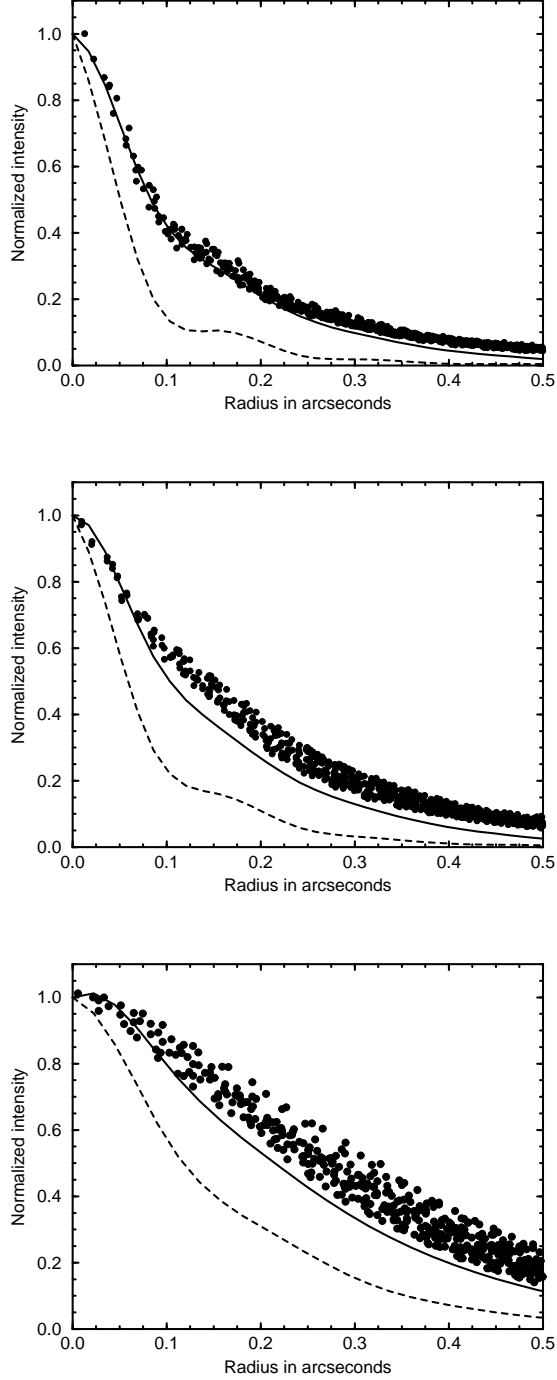


Fig. 7.— Plots of the PSFs in M 5 (CFHT) in mosaic 2 restored with the mosaic 1 kernel map. Shown are offsets of (top to bottom)  $0''$ ,  $15''$ , and  $25''$ . The filled circles are the data from mosaic 2. The dashed curves represent the normalized radial profiles of the PSFs at the same locations from mosaic 1, and the solid curves represent the model PSFs.

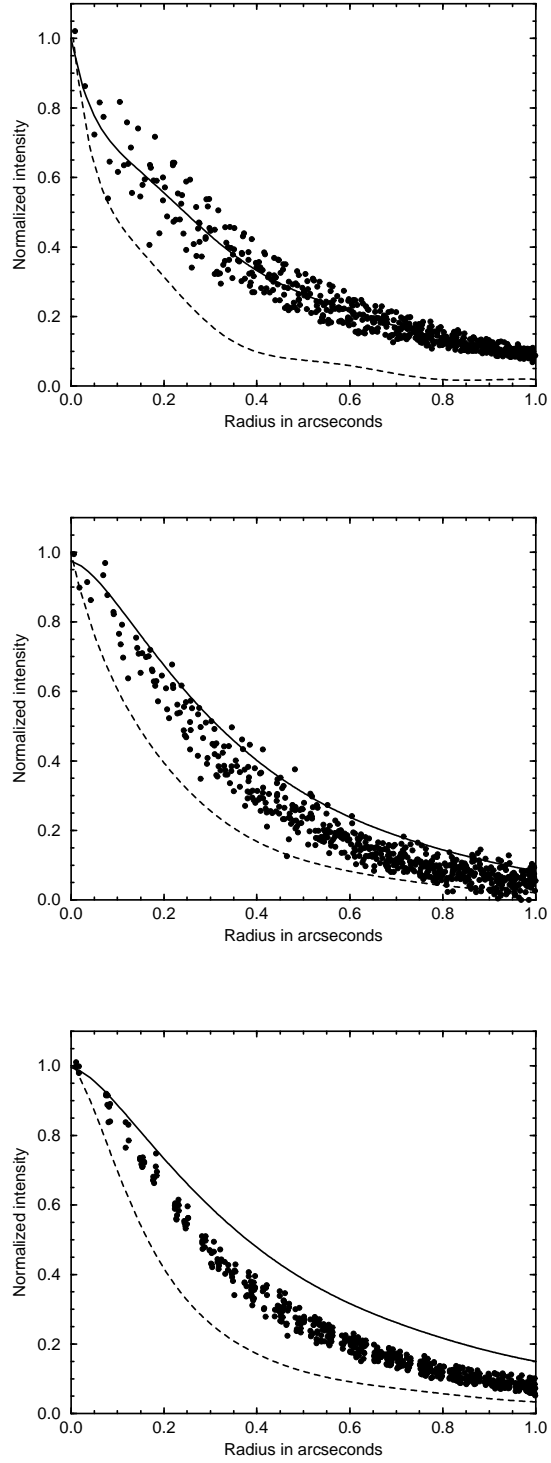


Fig. 8.— Plots of the PSFs in M 15 (Lick) in mosaic 2 restored with the mosaic 8 kernel map. The offsets and symbols are the same as Figure 7.

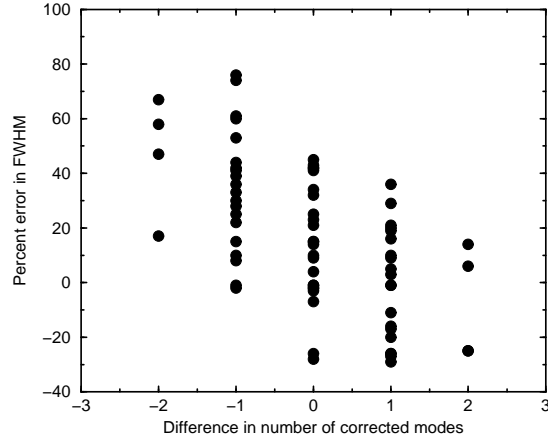


Fig. 9.— Plot of the percent error in predicting the FWHM as a function of the difference in number of corrected modes between the image used for the kernel map and the predicted image. Each of the kernel maps has been used to predict the PSF at an offset of  $25''$  in each of the other mosaics. Negative values on the axis correspond to a smaller number of corrected modes for the mosaic used to generate the kernel map. This plot suggests that for maximum accuracy the number of corrected modes should be similar, or larger in the kernel mosaic.